Identifying the Active Site in Nitrogen-Doped Graphene for the VO^{2+}/VO_2^{+} Redox Reaction

Jutao Jin,[†,‡] Xiaogang Fu,[†,§] Qiao Liu,[†,‡] Yanru Liu,[†] Zhiyang Wei,[†] Kexing Niu,[†] and Junyan Zhang[†,*]

[†]State Key Laboratory of Solid Lubrication, Lanzhou Institute of Chemical Physics, Chinese Academy of Sciences, Lanzhou 730000, People's Republic of China, [‡]University of Chinese Academy of Sciences, Beijing 100049, People's Republic of China, and [§]State Key Laboratory of Applied Organic Chemistry, College of Chemistry and Chemical Engineering, Lanzhou University, Lanzhou 730000, People's Republic of China

ABSTRACT Nitrogen-doped graphene sheets (NGS), synthesized by annealing graphite oxide (GO) with urea at 700−1050 °C, were studied as positive electrodes in a vanadium redox flow battery. The NGS, in particular annealed at 900 °C, exhibited excellent catalytic performance in terms of electron transfer (ET) resistance (4.74 ± 0.51 and $7.27 \pm 0.42\ \Omega$ for the anodic process and cathodic process, respectively) and reversibility ($\Delta E = 100$ mV, $I_{pa}/I_{pc} = 1.38$ at a scan rate of 50 mV s^{-1}). Detailed research confirms that not the nitrogen doping level but the nitrogen type in the graphene sheets determines the catalytic activity. Among four types of nitrogen species doped into the graphene lattice including pyridinic-N, pyrrolic-N, quaternary nitrogen, and oxidic-N, quaternary nitrogen is verified as a catalytic active center for the $[VO]^{2+}/[VO_2]^{+}$ couple reaction. A mechanism is proposed to explain the electrocatalytic performance of NGS for the $[VO]^{2+}/[VO_2]^{+}$ couple reaction. The possible formation of a N−V transitional bonding state, which facilitates the ET between the outer electrode and reactant ions, is a key step for its high catalytic activity.

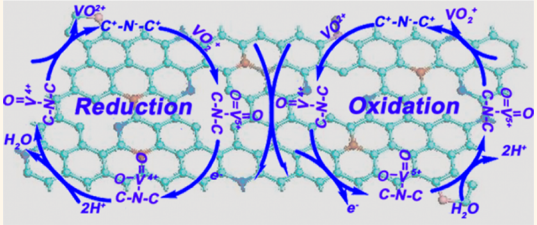

KEYWORDS: graphene sheets · nitrogen doping · $[VO]^{2+}/[VO_2]^{+}$ couple reaction · redox flow battery

The concerns about environmental pollution from the use of fossil fuels and resource constraints, as well as energy security, have spurred great interest in generating electric energy from renewable sources, such as solar and wind energy.[1,2] However, their intermittent nature makes solar and wind energy unreliable power sources. The integration of intermittent renewable energy into the electrical grid in the future is highly dependent on the development and compatibility of energy storage technologies with the current grid superstructure.[3] Electrochemical storage technologies that can efficiently store electricity in chemicals and reversibly release it according to demand are permissive technologies to store the intermittent energy from the sun and wind.[4] Distributed electrochemical storage technologies currently under development include redox flow batteries,[5] sodium−sulfur batteries,[6] and Li-ion batteries.[7] Among these energy storage technologies, the vanadium redox flow battery (VRFB) has been considered as a competitive and promising grid energy storage system for renewable energy due to its low cost, high efficiency, and good cycling stability.[8]

A VRFB is a battery that can store energy in vanadium-based redox couples and reversibly convert them into electrical energy.[8] The $[VO]^{2+}/[VO_2]^{+}$ (cathode) and V^{2+}/V^{3+} (anode) redox couples play key roles in the VRFB system to store chemical energy and convert it to electrical energy, in which the reaction kinetics of these two redox couples determine the efficiency of the whole cell. To ensure the cell runs with high efficiency, electrocatalysts are needed on both sides of the electrode to enhance the reversibility of the redox couples.[9] Traditionally, carbon-based materials with a graphite phase serve as both anode and cathode to collect electrons and catalyze the redox couples.[10−14] However, the electrode based on pure carbon materials has shown poor kinetic reversibility, especially on the cathodic side since the $[VO]^{2+}/[VO_2]^{+}$ couple reaction is complex, involving several elementary steps. Noble metal-based catalysts have shown higher catalytic activity for the $[VO]^{2+}/[VO_2]^{+}$

* Address correspondence to zhangjunyan@licp.cas.cn.

Received for review October 9, 2012 and accepted May 6, 2013.

10.1021/nn3046709

couple reaction, but they are not cost-effective.[15−17] Therefore, the exploration of low-cost and durable catalysts for efficient $[VO]^{2+}/[VO_2]^+$ couple reaction is paramount for further wide applications of VRFB.

Graphene, as a result of its unique two-dimensional monolayer structure of sp^2-hybridized carbon, has attracted interest in a wide range of fields, such as sensors, batteries, and catalysts.[18−20] Recently, reduced graphene oxide (RGO) or GO has been investigated as an electrode for VRFB.[21−24] It is proposed that the residual hydroxyl and carboxyl acid groups on graphene sheets (GS) served as active sites for the $[VO]^{2+}/[VO_2]^+$ couple reaction.[14,21,22] However, the drawback is the difficulty to balance the electron conductivity and catalytic activity of these GS- or GO-based catalysts, since improving the conductivity of RGO means the removal of hydroxyl and carboxyl acid groups on GS, which inversely unavoidably reduces the number of catalytic active site and lowers catalytic activity.[21,24] Recently, Penguin Han *et al*. fabricated a graphene oxide/carbon nanotube composite as an electrocatalyst for the $[VO]^{2+}/[VO_2]^+$ couple reaction,[22] where the carbon nanotube acted as the electroconductor and graphene oxide served as catalytic sites. Can we create active sites on GS for the $[VO]^{2+}/[VO_2]^+$ couple reaction without damaging the electron conductivity? Doping is an efficient way to tailor the electronic structure of materials and has been widely applied in nanocarbon materials, including graphene and carbon nanotubes, to improve their performances.[25−39] In particular, nitrogen, with high electron negativity, adjacent to carbon, could create positively charged carbon, which facilitates the adsorption of small molecules (O_2) on positively charged carbon atoms or cationic ions (Li^+, Na^+, K^+) on negatively charged nitrogen atoms to improve their intrinsic performance.[38,25,39] Recently, some attention has been paid to the potential applications of nitrogen-doped carbon as a cathodic catalyst of VRFB.[40,41] However, the role of nitrogen species for the $[VO]^{2+}/[VO_2]^+$ couple reaction is still unclear. Herein, we have synthesized nitrogen-doped graphene sheets (NGS) by annealing GO with urea and found that the catalytic activity of a nitrogen-doped NGS electrode for $[VO]^{2+}/[VO_2]^+$ couple reaction is much higher than an undoped GS electrode in terms of the results of electrocatalytic kinetics and reversibility. A detailed investigation revealed that quaternary nitrogen, stable in acidic solutions, acted as the most active sites for the $[VO]^{2+}/[VO_2]^+$ couple reaction. The enhanced catalytic activity of NGS for the $[VO]^{2+}/[VO_2]^+$ couple reaction may result from the change of the electron density and new created localized states in the NGS system induced by nitrogen doping, which facilitates the absorption of $[VO]^{2+}$ and $[VO_2]^+$ ions on the nitrogen dopant and the conjugation of the electron of the reactant into these localized states, similar to the previously observed ORR process on nitrogen-doped nanocarbons.[32,42] The finding is believed to be of tremendous assistance for the designing of novel efficient positive electrode catalysts, and we expect this work would provide valuable support for developing new advanced electrode materials for VRFB.

RESULTS AND DISCUSSION

GO was synthesized from graphite powder using an improved method.[43] NGS were obtained by annealing GO with urea under an Ar atmosphere for three hours in a tubular furnace. For comparison, undoped GS was also prepared under the same experimental conditions but without urea. Different annealing temperatures were used to tune the nitrogen content and bonding configuration in the NGS. The resulting materials annealed at 700, 800, 900, 1000, and 1050 °C are denoted as NGS-T (T = 700, 800, 900, 1000, and 1050 °C), respectively. All of the as-prepared samples were collected and characterized by scanning electron microscopy (SEM), transmission electron microscopy (TEM), X-ray powder diffraction (XRD), Raman spectroscopy, and X-ray spectroscopy (XPS).

Figure 1a and b show the typical microstructure of as-prepared sample NGS-900. The SEM image shows a flake-like morphology (Figure 1a). The detailed TEM image reveals that the flake-like layers are wrinkled rather than flat like GO (Figure 1b). Other samples show similar morphological characteristics (Figure S1). The wrinkling could be attributed to the local stress induced by the loss of oxygen and the introduction of nitrogen in NGS, like the wrinkling in the nitrogen-doped fullerene-like carbon.[44,45] Figure 1c shows the XRD patterns of NGS and undoped GS-900 after being annealed at 900 °C in Ar for three hours. In the case of undoped GS-900, GO's typical peak at 10.7° disappears completely, while a weak and broad diffraction peak (full width at half-maximum $B = 0.082$ rad) appears at 26.1° (layer distance $d = 0.36$ nm), suggesting that GO is partially reduced. With NGS-T obtained by annealing GO with urea, a relatively strong and narrow peak at 26.7° ($d = 0.34$ nm) corresponding to the diffraction of graphite (002) emerges. These results demonstrate that GO is well reduced when annealing with urea. Other NGS samples annealed at different temperatures also exhibit the (002) peak position at 26.7°, while the full width at half-maximum (B) increases with temperature. Thus it can be concluded that GO has been completely reduced at 700 °C, and further increasing the annealing temperature cannot improve the reduction degree but reduces the in-plane crystal size of NGS.[46]

Raman spectroscopy was also conducted to further identify the microstructure of the as-prepared samples. Figure 1d displays the Raman spectra of NGS and GS, where in all samples there is a G band centered at about 1590 and a D band at 1360. The G band arises from the stretching of the C−C sp^2 bond, while the D band is associated with the sp^3 defect sites.[47] Although there are no significant changes in the positions of the D and G bands, NGS (except NGS-700) shows a higher

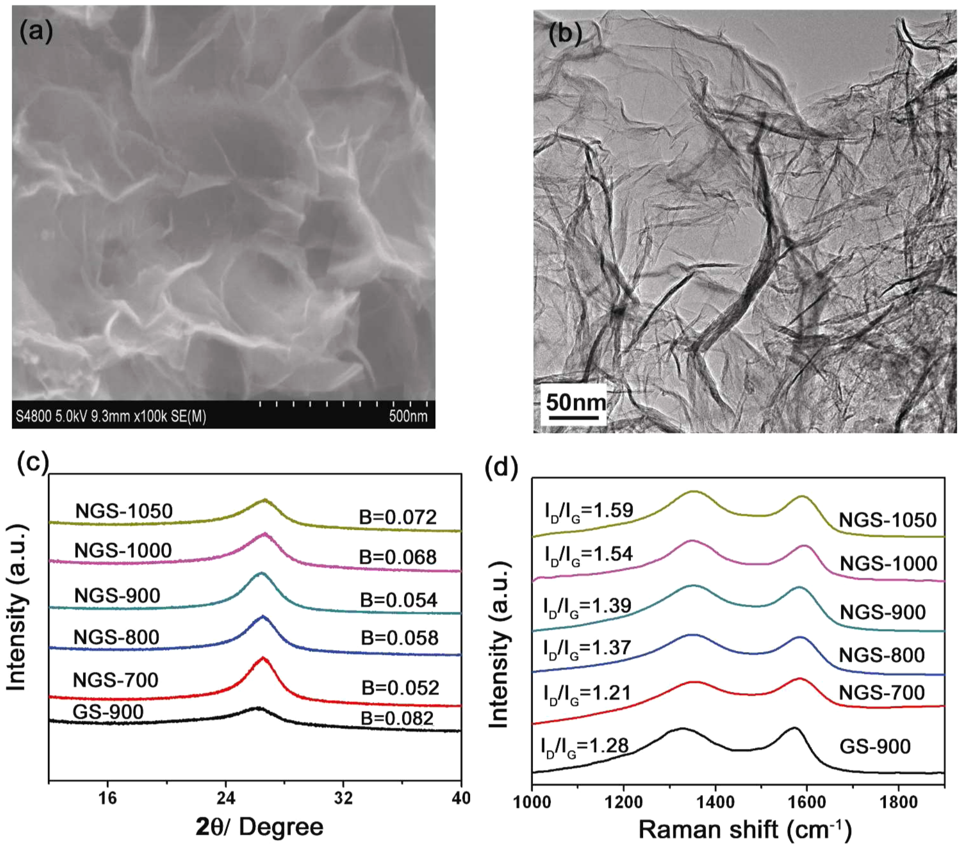

Figure 1. Characterization of as-prepared samples: (a) SEM image of NGS-900, (b) TEM image of NGS-900, (c) XRD patterns of NGS-T and GS-900, (d) visible-Raman spectra of NGS-T and GS-900.

intensity ratio of D band to G band, I_D/I_G, compared with GS, owing to the introduction of defects by N-doping (defects may include bonding disorders and vacancies in the graphene lattice introduced by nitrogen doping).[48] Notably, the I_D/I_G ratio of NGS gradually increases upon raising the annealing temperature, suggesting that a higher annealing temperature may induce more defects on the graphitic planes especially at high temperatures (>900 °C), which is consistent with the XRD results.

The elemental compositions and nitrogen-bonding configurations in these NGS-T samples were investigated *via* XPS. It is clear that the nitrogen band emerges in NGS, while it is absent in GS, indicating that nitrogen is successfully doped into GS. The atomic contents of carbon, nitrogen, and oxygen in the samples calculated from the XPS spectra (Figure 2a) are summarized in Table 1. The oxygen content of NGS-T (about 3 at. %) is much lower than that of GS-900 (about 12 at. %), further indicating the good reduction of GO with urea. The nitrogen doping level is sensitive to the annealing temperature, such that higher temperatures lead to lower doping levels (Table 1), which may originate from the cracking of unstable C–N bonds and the removal of nitrogen at elevated temperature. Urea has two functions in the formation of NGS. First, GO is exfoliated and reduced to GS with the help of gas produced by the pyrolysis of urea. Actually, urea has been used as an expansion–reduction agent to produce graphene from GO.[49] Second, although the

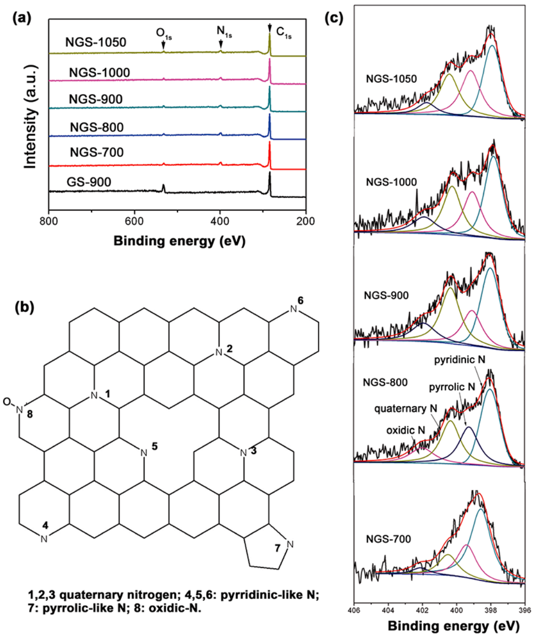

Figure 2. (a) XPS spectra of the NGS-T and GS-900 samples. (b) Schematic structure of NGS-T. (c) High-resolution N 1s spectra of NGS-T.

TABLE 1. Surface Species Content of NGS-T and GS Samples by XPS Results

	species concentration (at. %)		
	C	O	N
GS-900	88.08 ± 1.35	11.92 ± 1.07	
NGS-700	85.27 ± 1.09	4.61 ± 0.22	10.12 ± 0.88
NGS-800	87.67 ± 0.69	3.21 ± 0.20	9.11 ± 0.80
NGS-900	89.24 ± 0.51	3.14 ± 0.17	7.62 ± 0.59
NGS-1000	92.57 ± 0.67	3.42 ± 0.44	4.01 ± 0.10
NGS-1050	94.29 ± 0.43	3.52 ± 0.30	2.19 ± 0.18

TABLE 2. N Species Content of NGS-T Samples by XPS

	N species content (at. %)			
	pyridinic-N	pyrrolic-N	quarternary N	oxidic-N
NGS-700	48.56 ± 0.46	21.42 ± 0.11	17.78 ± 0.53	12.24 ± 1.10
NGS-800	40.43 ± 0.23	22.62 ± 0.53	23.41 ± 0.44	13.54 ± 0.15
NGS-900	35.37 ± 0.41	20.59 ± 0.44	31.46 ± 0.50	12.58 ± 0.47
NGS-1000	36.65 ± 0.69	23.73 ± 0.29	27.65 ± 0.48	11.97 ± 0.50
NGS-1050	35.31 ± 0.42	24.68 ± 0.32	27.52 ± 0.31	12.49 ± 1.06

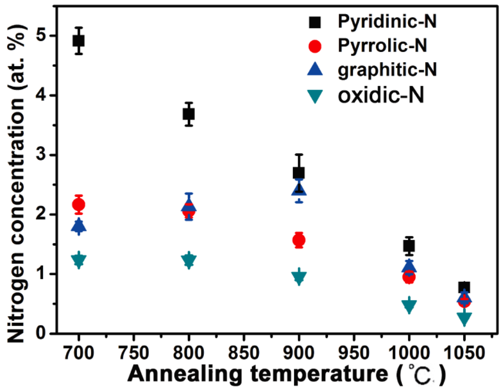

Figure 3. Nitrogen species concentration *versus* annealing temperature.

pyrolysis temperature of urea is as low as about 180 °C,[50] its decomposition products, including cyanuric acid and melamine, can polymerize into more stable graphite-like carbon nitride (Figure S1a).[51,52] The polymerized carbon nitride then decomposes to produce NH$_3$ at temperatures above 600 °C, which is beneficial for nitrogen doping.[46] Notably, unlike annealing GO in an NH$_3$ atmosphere, which may lead to only a low level of surface doping (N content: 3.5 at. % at 800 °C),[46] a large amount of NH$_3$ generated from the decomposition of urea or the polymerized carbon nitride can filter into the inner space of the GO layers and result in a homogeneously higher nitrogen doping level (nitrogen content: 9.11 ± 0.80 at. % at 800 °C).

The bonding configurations of nitrogen in NGS were further studied on the basis of high-resolution XPS spectra. Figure 2c shows the N 1s spectra of NGS. The N 1s band can be deconvoluted into four bands at 398.3, 399.8, 400.9, and 402.9 eV, assigned to nitrogen atoms in the pyridinic N−C structure, pyrrolic-N−C structure, quaternary N−C structure, and oxidic-N of pyridinic-N, respectively.[53,54] The molecular bonding structures are depicted in Figure 2b. The quaternary-N is a type of nitrogen that bonds to three carbon atoms in the plane of the graphene matrix. Pyridinic-N refers to a nitrogen atom at the edge of GS (including edges created by vacancy defects). Pyrrolic-N is a nitrogen atom incorporated into five-membered heterocyclic rings. Oxidic-N is a nitrogen atom bonded with two carbon atoms and one oxygen atom. The relative content of each nitrogen species is listed in Table 2. With increasing the annealing temperature from 700 to 900 °C, the relative content of pyridinic-N decreases from 48.56 ± 0.46% to 35.37 ± 0.31%, while the quaternary nitrogen content increases from 17.78 ± 0.53% to 31.46 ± 0.50%. Upon further increasing the annealing temperature from 900 to 1050 °C, the pyridinic-N and quaternary nitrogen content remains at 35% and 30%, respectively. Almost no change is observed for the contents of pyrrolic-N and oxidic-N within annealing temperatures from 700 to 1050 °C. Considering the fact that the total concentration of nitrogen in NGS changes with annealing temperature, it is worthwhile to study the absolute concentration of these nitrogen species (calculated by multiplying the relative atomic content of each nitrogen species and total nitrogen concentration) in NGS. We plot the nitrogen species concentration *versus* annealing temperature in Figure 3, where the concentrations of all the nitrogen species except quaternary nitrogen decrease with an increase in the annealing temperature from 700 to 1050 °C. It is worth special notice that the concentrations of all nitrogen species including quaternary nitrogen drop with an accelerated rate above 900 °C. These results demonstrate that pyridinic-N, pyrrolic-N, and oxidic-N become unstable above 700 °C. In the case of quaternary nitrogen, its concentration first increases upon raising the annealing temperature, reaches a maximum concentration of 2.39 ± 0.19 at. % at 900 °C, and then rapidly shifts down to 0.81 ± 0.09 at. % at 1050 °C. These results demonstrate that the destruction and reconstruction processes of nitrogen species have happened during the annealing process. The increase of the quaternary nitrogen concentration from 700 to 900 °C might originate from the conversion of other nitrogen species in NGS, mainly pyridinic-N, as previously found in other materials.[32,55] Further increasing the annealing temperature above 900 °C would make all of the nitrogen species in NGS unstable, leading to the removal of nitrogen dopant and the formation of defects. The bonding configurations of carbon and oxygen are also analyzed in the Supporting Information (see Figure S2).

Cyclic voltammetry (CV) was conducted to assess the catalytic activity of NGS toward the redox [VO]$^{2+}$/[VO$_2$]$^+$

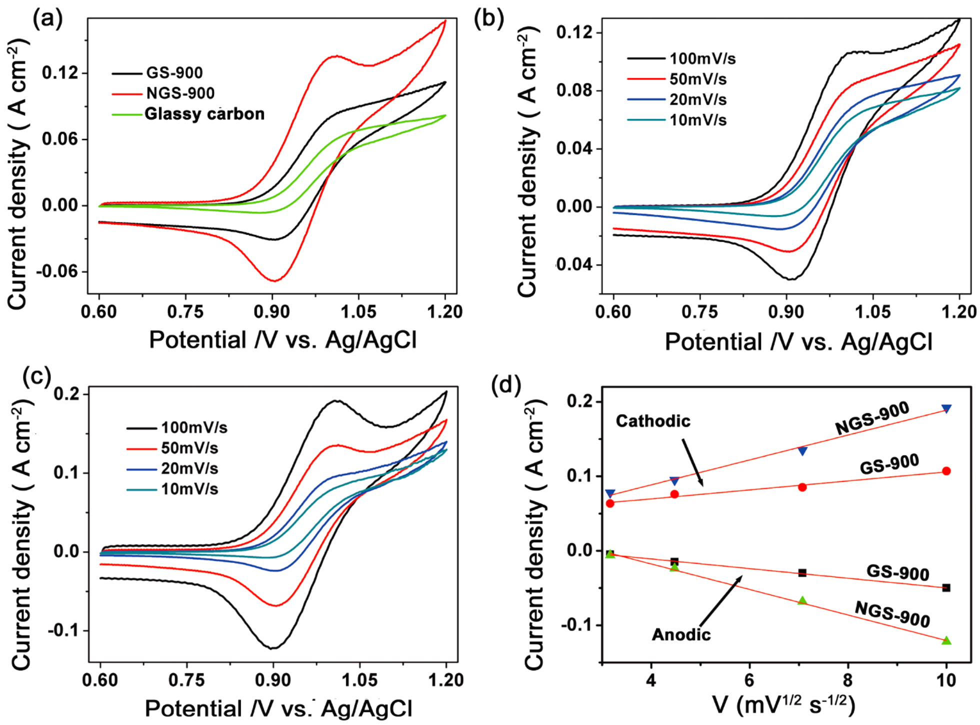

Figure 4. (a) Cyclic votammograms on different electrodes in 1 mol L^{-1} VOSO$_4$ + 3 mol L^{-1} H$_2$SO$_4$ solutions at a scan rate of 50 mV s^{-1}. Cyclic votammograms in 1 mol L^{-1} VOSO$_4$ + 3 mol L^{-1} H$_2$SO$_4$ solutions (b) on the GS-900 electrode and (c) on the NGS-900 electrode. (d) Plot of peak current density *versus* square of scan rate.

couple reaction in 1 mol L^{-1} VOSO$_4$ + 3 mol L^{-1} H$_2$SO$_4$ solutions. As shown in Figure 4a, the typical redox peaks corresponding to the redox couple reaction in eq 1 appear on the CV curves of GS-900 and NGS-900 electrodes, while no obvious redox peak is observed on the pure glassy carbon electrode, demonstrating that the catalytic activity originates from the catalysts (CV curves of NGS annealing at other temperatures are also shown in Figure S3). The GS-900 electrode shows an anodic peak potential (V_{pa}) at 1.02 V and a cathodic peak potential at 0.90 V, along with an anodic (I_{pa}) and a cathodic peak current density (I_{pc}) of 0.086 ± 0.004 and 0.051 ± 0.002 A cm^{-2}, respectively. Compared with GS-900, the NGS-900 electrode shows a little negative shift of V_{pa} to 1.00 V and a similar V_{pc} at 0.90 V, accompanied by the increase of I_{pa} to 0.135 ± 0.014 A cm^{-2} and I_{pc} to 0.097 ± 0.011 A cm^{-2}, respectively. The relatively higher redox peak current density of I_{pa} and I_{pc} on the NGS-900 electrode suggests more favorable electron transfer (ET) kinetics for the [VO]$^{2+}$/[VO$_2$]$^+$ redox couple reaction than on GS-900.

$$[VO]^{2+} + H_2O \overset{\text{catalyst (NGS)}}{\rightleftharpoons} [VO_2]^{+} + 2H^{+} + e^{-} \qquad (1)$$

We further evaluated the reversibility of the redox reaction [VO]$^{2+}$/[VO$_2$]$^+$ by calculating the peak potential separation (ΔE) and the ratio of the redox peak current density (I_{pa}/I_{pc}) at different scan rates, two important factors related to the reversibility of the redox reaction. The peak current density I_{pa} and I_{pc} and peak potential V_{pa} and V_{pc} on the NGS-900 and GS-900 electrodes at different scan rates are obtained from Figure 4b and c. The value of ΔE on NGS-900 is about 100 mV at a scan rate of 50 mV s^{-1} and remains almost constant at different scan rates. In contrast, GS-900 shows a larger ΔE value at the same experimental conditions. As for I_{pa}/I_{pc}, the values for NGS-900 and GS-900 are 1.38 and 1.69, respectively, at a scan rate of 50 mV s^{-1}. Though I_{pa}/I_{pc} increases on both NGS-900 and GS-900 electrodes with decreasing scan rate, NGS-900 shows a lower I_{pa}/I_{pc} value than GS-900. Combining the value of ΔE and I_{pa}/I_{pc}, we can conclude that NGS-900 possesses a relatively better reversibility for the [VO]$^{2+}$/[VO$_2$]$^+$ redox reaction than GS-900.

The mass transfer (MT) property is estimated by plotting the redox current density *versus* the square root of the scan rate (Figure 4d). The redox current is proved to be nearly proportional to the square root of the scan rate on both GS-900 and NGS-900 electrodes. Nevertheless, the slope of NGS-900 is larger than that of GS-900 for both cathodic and anodic processes, suggesting a faster MT process on the surface of NGS-900. The relatively faster MT process on the surface of NGS-900 may originate from the lower surface energy of NGS-900 induced by the nitrogen doping. The hydrophilic properties of all samples were tested and are shown in Figure S4. All of nitrogen-doped graphene except NGS-1050 shows a contact angle of about 13.5°, compared with 38.4° for GS-900. The relatively larger contact angle of NGS-1050 (21.1°) may contribute to its low nitrogen-doping level. The enhanced hydrophilic property of NGS and their low surface energy could facilitate ion transport, as confirmed by previous reports.[28,40]

Electrical impedance spectroscopy (EIS) was used to further investigate the ET process and thereby further evaluate the catalytic activity of these catalysts. Figure 5 shows the Nyquist plots at 0.90 and 1.00 V for the reduction and oxidation processes of $[VO]^{2+}/[VO_2]^+$, respectively. The intercept on the real axis is the ohmic resistance (R_s), attributed to the solution, electrode, and contact resistance. The left arch (high-frequency range) can be assigned to the ET resistance (R_{ct}) and corresponding electric double-layer capacitance (Q_1) of the electrode–electrolyte interface, while the right arch (low-frequency range) can be assigned to the Nernst diffusion impedance (Q_2) of the redox couple $[VO]^{2+}/[VO_2]^+$. $Q_1 = Y_{0,1}{}^{-1}(j\omega)^{-n_1}$, and $Q_2 = Y_{0,2}{}^{-1}(j\omega)^{-n_2}$ where $Y_{0,1}$ ($Y_{0,2}$) and n_1 (n_2) are the prefactor and exponent of Q_1 (Q_2), respectively. The EIS data are obtained by fitting the Nyquist plots with an equivalent circuit diagram, and the results are summarized in Table 3. For the GS-900 electrode, the R_{ct} values corresponding to the reduction and oxidation processes are 21.76 ± 1.18 and 11.69 ± 0.55 Ω, respectively. For the NGS-900 electrode, they reduce to 7.27 ± 0.42 and 4.74 ± 0.51 Ω, respectively. These results further demonstrate that NGS-900 provides a much smoother ET channel than the GS-900 electrode for the $[VO]^{2+}/[VO_2]^+$ redox couple reaction. Meanwhile, NGS-900 holds a larger $Y_{0,2}$ value and similar $Y_{0,1}$ value compared with GS-900 for both the oxidation and reduction processes. The larger $Y_{0,2}$ value indicates a higher MT rate of $VO_2{}^+$ or VO^{2+} ions through the pore channel of the electrode, and the similar $Y_{0,1}$ value suggests that NGS-900 and GS-900 have a similar electrode–electrolyte interface.[56] From the above results, we can conclude that the higher catalytic activity of the $[VO]^{2+}/[VO_2]^+$ redox couple reaction on NGS-900 can be attributed to the combined action of faster ET and MT rates, consistent with the CV results. The high MT rate is probably due to the low surface energy and enhanced hydrophilic property of NGS-900 by nitrogen doping. As for the ET rate, the enhanced ET rate of NGS-900 might originate from the nitrogen dopant, similar to the oxygen dopant in GS,[21,22] accelerating the ET rate for the $[VO]^{2+}/[VO_2]^+$ reaction. The fact that NGS-900 contains a higher nitrogen and lower oxygen content than GS-900 suggests that the nitrogen dopant is the catalytically active component, whereas the catalytic contribution from the oxygen dopant cannot be excluded completely. It should be particularly noted that the ET resistance R_{ct} of the reduction process is much larger than that of the oxidation process for both GS-900 and NGS-900 electrodes, suggesting faster ET kinetics of the reduction process than the oxidation process for the $[VO]^{2+}/[VO_2]^+$ couple reaction. This result is consistent with the CV result that I_{pc} is smaller than I_{pa} on both NGS-900 and GS-900 electrodes.

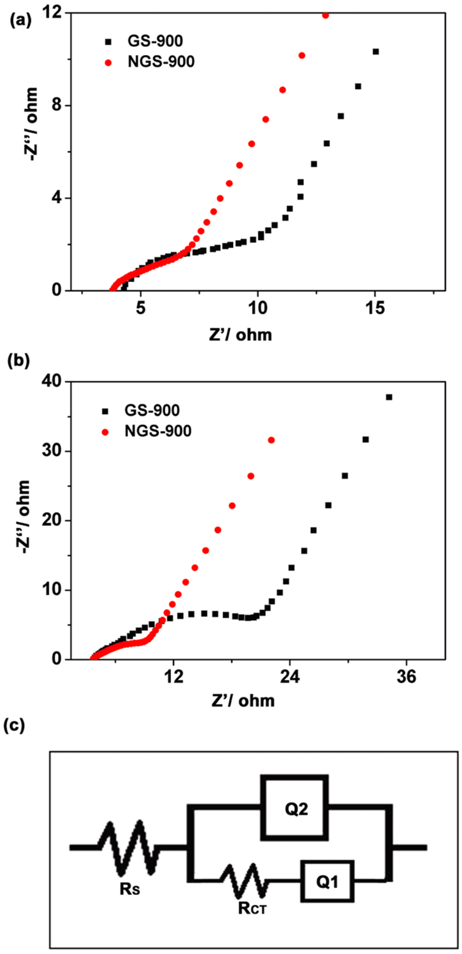

Figure 5. Nyquist spectra of electrochemical impedance spectra of the NGS-900 and GS-900 electrodes obtained in 1 mol L^{-1} $VOSO_4$ + 3 mol L^{-1} H_2SO_4 solutions at the (a) anodic potential of 1.0 V and (b) cathodic potential of 0.9 V. (c) Corresponding equivalent circuit representing the circuit elements in the Nyquist spectra.

To examine the mechanism of NGS on the $[VO]^{2+}/[VO_2]^+$ redox couple reaction, the catalytic activity of NGS prepared at different temperatures have been investigated (Figure S5). The catalytic activity of NGS in terms of peak current density decreases in the order NGS-900 > NGS-700 > NGS-800 > NGS-1000 > NGS-1050, while the total nitrogen content of NGS-T, according to the XPS results, decreases in the order NGS-700 > NGS-800 > NGS-900 > NGS-1000 > NGS-1050. Obviously, the catalytic activity of NGS is independent of the nitrogen content. In order to probe which nitrogen species is the active site, the plots of the concentration of each nitrogen species *versus* the peak current density are given in Figure 5. A good linear relationship between the concentration of quaternary nitrogen and the peak current density (for both anodic and cathodic electrodes) is obtained, but no direct correlation can be established for the other three kinds of species: pyridinic-N, pyrrolic-N, and oxidic-N (Figure S5). Thus, it is reasonable to conclude that the quaternary nitrogen species is the active site for the $[VO]^{2+}/[VO_2]^+$ redox couple reaction.

TABLE 3. Fit Parameters Resulting from the Equivalent Circuit Model in Figure 4

			Q_1 (CPE)			Q_2 (CPE)	
		R_s (ohm)	$Y_{0,1}$ (10^{-3})	n_1	R_{ct} (ohm)	$Y_{0,2}$ (10^{-3})	n_2
NGS-900	anodic	3.73 ± 0.11	6.01 ± 0.21	0.76 ± 0.03	4.74 ± 0.51	3.67 ± 0.12	0.57 ± 0.08
	cathodic	3.68 ± 0.12	5.91 ± 0.13	0.75 ± 0.06	7.27 ± 0.42	2.78 ± 0.23	0.62 ± 0.04
GS-900	anodic	3.81 ± 0.20	1.89 ± 0.09	0.83 ± 0.02	11.69 ± 0.55	4.05 ± 0.01	0.48 ± 0.09
	cathodic	3.71 ± 0.32	2.62 ± 0.11	0.80 ± 0.03	21.76 ± 1.18	2.76 ± 0.06	0.65 ± 0.07

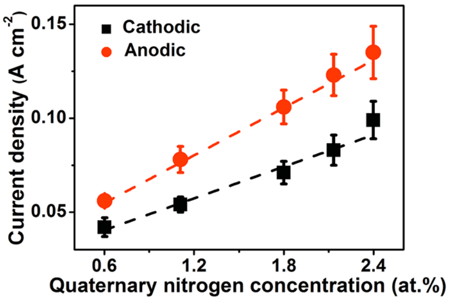

Figure 6. Relationship between peak current density and concentration of quaternary nitrogen species.

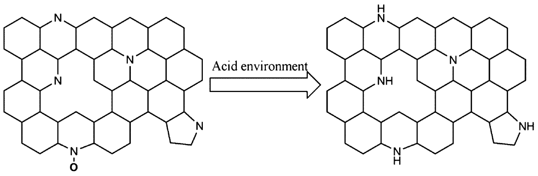

Scheme 1. Protonation reaction of different nitrogen species in an acidic environment.

As mentioned above, four types of nitrogen species in the graphene matrix are in different bonding environments and show different electronic structure. Both pyridinic-N and pyrrolic-N are bonded to two carbon atoms and contribute one and two p electrons to the π system, respectively, generating a lone pair of electrons on the nitrogen atom. In an acidic environment, the lone pair of electrons localized around the nitrogen atom can be protonized to N$-$H (Scheme 1). In addition, oxidic-N in the graphene matrix can be converted to pyridinic-N first and then to pyridinic-N$-$H in an acidic environment (Scheme 1).[57] Nitrogen in pyridinic-N and pyrrolic-N configurations bears a higher negative charge density than quaternary nitrogen, which is more favorable for the adsorption of positively charged ions in solutions. However, the protonation reaction of these nitrogen species in an acidic environment may make them inactive for the $[VO]^{2+}/[VO_2]^+$ redox reaction. In contrast, the quaternary nitrogen-substituted carbon atom in the graphene matrix and all electrons are delocalized into the π system of GS without a lone electron pair around the quaternary nitrogen. Thus, the quaternary nitrogen is more stable in an acidic environment since it is less susceptible to protonization. Therefore, the quaternary nitrogen atoms in NGS act as active sites for the $[VO]^{2+}/[VO_2]^+$ redox reaction.

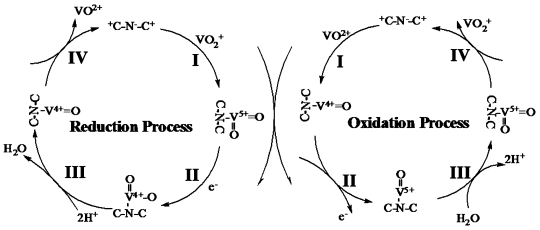

Scheme 2. Proposed catalytic mechanism of NGS for the $[VO]^{2+}/[VO_2]^+$ redox reaction.

The mechanism for the catalytic process of the $[VO]^{2+}/[VO_2]^+$ redox couple reaction on NGS catalysts is proposed (Scheme2). The relatively high negative charge density of the incorporated nitrogen due to its strong electronegativity[38] would promote the adsorption process of positively charged reactant ions, including VO_2^+ and VO^{2+} on the active sites. Furthermore, the additional electron of nitrogen can create localized states around the nitrogen dopant in GS,[58] which may match the empty molecular orbital of VO_2^+ or VO^{2+} to form a N$-$V transitional state and facilitate the ET between the reactants and the catalysts (first step). During the catalytic process, with the electrode potential negatively (positively) shifted, the electron on the electrode transfers into (out off) the antibonding orbital of VO_2^+ (VO^{2+}) through N$-$V bonding (second step). For the reduction process, the additional electron in the antibonding orbital of VO_2^+ weakens the V=O bond and removes one of the oxygens with two protons (third step for the reduction process). For the oxidation process, one H_2O molecule coordinates with the empty orbital of VO^{2+} to generate a VO_2^+ and two protons (third step for the oxidation process). Lastly, the VO^{2+} or VO_2^+ is removed from the active site. Among the four steps, we think that the first step is the rate-determining step for both the oxidation process and reduction process. The higher ET resistance of GS-900 is likely due to the fact that the reactant ions are difficult to be adsorbed on the active site and the electrons of the reactant cannot easily conjugate into the delocalized p bonding of graphene because of the mismatch.

CONCLUSION

In summary, we synthesized nitrogen-doped graphene by a simple and scalable method and studied its catalytic activity for the $[VO]^{2+}/[VO_2]^+$ redox couple reaction. The as-synthesized NGS-900 exhibited excellent catalytic activity, with an ET resistance of 4.74 ± 0.51 and 7.27 ± 0.42 Ω for the anodic and cathodic processes, respectively. We propose that the nitrogen dopant in GS facilitates the adsorption and coordination of the reactant ions on the active site, which results in a high catalytic activity. Among the four nitrogen species in GS, the quaternary nitrogen is more stable and serves as the active site for the $[VO]^{2+}/[VO_2]^+$ redox couple reaction. These findings would be of help to guide the design of high-activity catalysts by selectively doping GS with quaternary nitrogen. Furthermore, other heteroatoms, such as phosphorus-, boron-, or sulfur-doped graphene, may also show enhanced catalytic activity for the $[VO]^{2+}/[VO_2]^+$ redox couple reaction. The result in this work opens up a new avenue to fabricate positive electrocatalysts for vanadium redox flow batteries.

METHODS

Synthesis of NGS-T and GS. GO was prepared by oxidation of natural graphite powder (100 mesh, Qingdao Huatai Lubricant Sealing S&T Co. Ltd., Qingdao, China) according to an improved method.

To prepare nitrogen-doped graphene sheets, the as-prepared GO (100 mg) was thoroughly mixed with a solution of urea (200 mg) in ethanol (50 mL) by sonicating for 30 min. Then the mixture was heated to 80 °C and stirred in a 250 mL beaker until dried. The dried samples were put in a covered crucible in the center of a tube furnace. Then, the furnace was pumped with a rotary pump to 10 Pa and washed with Ar three times to completely remove oxygen in the tube furnace. After that, the temperature of the furnace was raised to 600 °C at a heating rate of 3 °C min^{-1} and maintained for one hour under Ar flow (100 sccm). Then, the temperature of the furnace was rapidly raised to an appointed temperature with a heating rate of 5 °C min^{-1} and annealed three hours for preparation of NGS. Five annealing temperatures of 700, 800, 900, 1000, and 1050 °C were chosen to synthesize NGS with different nitrogen concentrations. After the furnace was naturally cooled to room temperature, the samples were collected for further characterization. GS without nitrogen doping was prepared by the same procedure but without adding urea to GO.

Characterization. TEM and HRTEM images were collected on a Tecnai-G2-F30 (300 keV) field emission transmission electron microscope; SEM images were recorded on a Hitachi S4800-F scanning electron microscope; the XPS spectrum was collected using a VG Scientific ESCALAB210-XPS photoelectron spectrometer with an Mg Kα X-ray resource; Raman spectra were collected with a Jobin Yvon T64000 Raman spectrometer with a 514.5 nm Ar laser as the excitation source. XRD patterns were recorded on a Rigaku B/Max-RB X-ray diffractometer with nickel-filtrated Cu Kα radiation (Cu Kα, λ = 1.5406).

Electrochemical Test. The electrochemical tests were carried out on an AutoLab workstation. Electrochemical measurements were conducted using a three-electrode electrochemical cell. A glassy carbon electrode coated with catalysts was used as working electrode. The catalysts-coated electrode was prepared as follows: 100 μL of 5 wt % Nafion solution was added in 1 mL of 4:1 v/v water/ethanol, and then 4 mg of catalyst was dispersed in the as-prepared solution by at least 60 min sonication to form a homogeneous suspension. Then 5 μL of the suspension was loaded onto a glassy carbon electrode of 3 mm in diameter with a mass loading of about 0.283 mg cm^{-2}. A Ag/AgCl electrode in saturated KCl aqueous solution and a platinum wire were used as reference and counter electrode, respectively. Cyclic voltammetry was conducted in 1 mol L^{-1} $VOSO_4$ + 3 mol L^{-1} H_2SO_4 solutions with a scanning rate of 10, 20, 50, and 100 mV s^{-1}, respectively. Electrochemical impedance spectroscopy was conducted in a 1 mol L^{-1} $VOSO_4$ + 3 mol L^{-1} H_2SO_4 solution at 0.90 and 1.00 V for the reduction and oxidation processes of $[VO]^{2+}/[VO_2]^+$, respectively. All experiments were conducted at room temperature (20 °C).

Conflict of Interest: The authors declare no competing financial interest.

Acknowledgment. We acknowledge J. W. Zhang of Lanzhou University for the Raman test. We also acknowledge Prof. J. Z. Zhao, L. He, and L. Gao at Lanzhou Institute of Chemical Physics, Chinese Academy of Sciences, for SEM, XRD, and XPS measurements, respectively. TEM was performed at Lanzhou University with the support of Prof. Y. Peng and Dr. Z. B. Gong. Funding was provided by the National Nature Science Foundation (NSFC) of China under award no. 50823008.

Supporting Information Available: Core level high-resolution C 1s (a) and O 1s (b) XPS spectra of NGS-T samples (Figure S1); cyclic voltammograms on NGS-T electrodes in 1 mol L^{-1} $VOSO_4$ + 3 mol L^{-1} H_2SO_4 (Figure S2); relationship between peak current density and concentration of N species: (a) pyridinic-N, (b) pyrrolic-N, (c) oxidic-N (Figure S3). This material is available free of charge *via* the Internet at http://pubs.acs.org.

REFERENCES AND NOTES

1. Johansson, T. B.; Burnham, L. *Renewable Energy: Sources for Fuels and Electricity*; Island Pr: 1993; pp 1−2.
2. Koroneos, C.; Spachos, T.; Moussiopoulos, N. Energy Analysis of Renewable Energy Sources. *Renewable Energy* **2003**, *28*, 295–310.
3. Yang, Z.; Liu, J.; Baskaran, S.; Imhoff, C. H.; Holladay, J. D. Enabling Renewable Energy—and the Future Grid—with Advanced Electricity Storage. *JOM J. Minerals, Met. Mater. Soc.* **2010**, *62*, 14–23.
4. Yang, Z.; Zhang, J.; Kintner-Meyer, M. C. W.; Lu, X.; Choi, D.; Lemmon, J. P.; Liu, J. Electrochemical Energy Storage for Green Grid. *Chem. Rev.* **2011**, *111*, 3577.
5. Huang, K. L.; Li, X.; Liu, S.; Tan, N.; Chen, L. Research Progress of Vanadium Redox Flow Battery for Energy Storage in China. *Renewable Energy* **2008**, *33*, 186–192.
6. Roberts, B. P. In *Sodium-Sulfur (NaS) Batteries for Utility Energy Storage Applications*; IEEE, 2008; pp 1−2.
7. Choi, D.; Wang, D.; Viswanathan, V. V.; Bae, I. T.; Wang, W.; Nie, Z.; Zhang, J. G.; Graff, G. L.; Liu, J.; Yang, Z. Li-Ion Batteries from $LiFePO_4$ Cathode and Anatase/Graphene Composite Anode for Stationary Energy Storage. *Electrochem. Commun.* **2010**, *12*, 378–381.
8. Ponce de León, C.; Frías-Ferrer, A.; González-García, J.; Szánto, D. A.; Walsh, F. C. Redox Flow Cells for Energy Conversion. *J. Power Sources* **2006**, *160*, 716–732.
9. Wu, X. W.; Yamamura, T.; Ohta, S.; Zhang, Q. X.; Lv, F. C.; Liu, C. M.; Shirasaki, K.; Satoh, I.; Shikama, T.; Lu, D. Acceleration of the Redox Kinetics of VO^{2+}/VO_2^{+} and V^{3+}/V^{2+}Couples on Carbon Paper. *J. Appl. Electrochem.* **2011**, *41*, 1–8.
10. Zhu, H. Q.; Zhang, Y. M.; Yue, L.; Li, W. S.; Li, G. L.; Shu, D.; Chen, H. Y. Graphite−Carbon Nanotube Composite Electrodes for all Vanadium Redox Flow Battery. *J. Power Sources* **2008**, *184*, 637–640.
11. Zhou, H.; Zhang, H.; Zhao, P.; Yi, B. A Comparative Study of Carbon Felt and Activated Carbon Based Electrodes for Sodium Polysulfide/Bromine Redox Flow Battery. *Electrochim. Acta* **2006**, *51*, 6304–6312.
12. Kim, K. J.; Kim, Y.-J.; Kim, J.-H.; Park, M.-S. The Effects of Surface Modification on Carbon Felt Electrodes for Use in Vanadium Redox Flow Batteries. *Mater. Chem. Phys.* **2011**, *131*, 547–553.

13. Radford, G. J. W.; Cox, J.; Wills, R. G. A.; Walsh, F. C. Electrochemical Characterisation of Activated Carbon Particles Used in Redox Flow Battery Electrodes. *J. Power Sources* **2008**, *185*, 1499–1504.
14. Yue, L.; Li, W.; Sun, F.; Zhao, L.; Xing, L. Highly Hydroxylated Carbon Fibres as Electrode Materials of All-Vanadium Redox Flow Battery. *Carbon* **2010**, *48*, 3079–3090.
15. Oriji, G.; Katayama, Y.; Miura, T. Investigation on V (IV)/V (V) Species in a Vanadium Redox Flow Battery. *Electrochim. Acta* **2004**, *49*, 3091–3095.
16. Gattrell, M.; Park, J.; MacDougall, B.; Apte, J.; McCarthy, S.; Wu, C. Study of the Mechanism of the Vanadium 4+/5+ Redox Reaction in Acidic Solutions. *J. Electrochem. Soc.* **2004**, *151*, A123–A130.
17. Wang, W. H.; Wang, X. D. Investigation of Ir-Modified Carbon Felt as the Positive Electrode of an All-Vanadium Redox Flow Battery. *Electrochim. Acta* **2007**, *52*, 6755–6762.
18. Robinson, J. T.; Perkins, F. K.; Snow, E. S.; Wei, Z. Q.; Sheehan, P. E. Reduced Graphene Oxide Molecular Sensors. *Nano Lett.* **2008**, *8*, 3137–3140.
19. Reddy, A. L. M.; Srivastava, A.; Gowda, S. R.; Gullapalli, H.; Dubey, M.; Ajayan, P. M. Synthesis of Nitrogen-Doped Graphene Films for Lithium Battery Application. *ACS Nano* **2010**, *4*, 6337–6342.
20. Liu, F.; Song, S.; Xue, D.; Zhang, H. Folded Structured Graphene Paper for High Performance Electrode Materials. *Adv. Mater.* **2012**, *24*, 1089–1094.
21. Han, P.; Wang, H.; Liu, Z.; Chen, X.; Ma, W.; Yao, J.; Zhu, Y.; Cui, G. Graphene Oxide Nanoplatelets as Excellent Electrochemical Active Materials for VO^{2+}/VO$_2^{+}$ and V^{2+}/V^{3+} Redox Couples for a Vanadium Redox Flow Battery. *Carbon* **2011**, *49*, 693–700.
22. Han, P.; Yue, Y.; Liu, Z.; Xu, W.; Zhang, L.; Xu, H.; Dong, S.; Cui, G. Graphene Oxide Nanosheets/Multi-Walled Carbon Nanotubes Hybrid as an Excellent Electrocatalytic Material towards VO^{2+}/VO$_2^{+}$ Redox Couples for Vanadium Redox Flow Batteries. *Energy Environ. Sci.* **2011**, *4*, 4710–4717.
23. Li, W.; Liu, J.; Yan, C. Graphite−Graphite Oxide Composite Electrode for Vanadium Redox Flow Battery. *Electrochim. Acta* **2011**, *56*, 5290–5294.
24. González, Z.; Botas, C.; Álvarez, P.; Roldán, S.; Blanco, C.; Santamaría, R.; Granda, M.; Menéndez, R. Thermally Reduced Graphite Oxide as Positive Electrode in Vanadium Redox Flow Batteries. *Carbon* **2012**, *50*, 828–834.
25. Jeong, H. M.; Lee, J. W.; Shin, W. H.; Choi, Y. J.; Shin, H. J.; Kang, J. K.; Choi, J. W. Nitrogen-Doped Graphene for High-Performance Ultracapacitors and the Importance of Nitrogen-Doped Sites at Basal Planes. *Nano Lett.* **2011**, *11*, 2472–2477.
26. Xiong, W.; Du, F.; Liu, Y.; Perez, A.; Supp, M.; Ramakrishnan, T. S.; Dai, L.; Jiang, L. 3-D Carbon Nanotube Structures Used as High Performance Catalyst for Oxygen Reduction Reaction. *J. Am. Chem. Soc.* **2010**, *132*, 15839–15841.
27. Yang, W.; Fellinger, T.-P.; Antonietti, M. Efficient Metal-Free Oxygen Reduction in Alkaline Medium on High-Surface-Area Mesoporous Nitrogen-Doped Carbons Made from Ionic Liquids and Nucleobases. *J. Am. Chem. Soc.* **2010**, *133*, 206–209.
28. Chen, L.-F.; Zhang, X.; Liang, H.-W.; Kong, M.; Guan, Q.-F.; Wu, Z.-Y.; Yu, S.-H. Synthesis of Nitrogen-Doped Porous Carbon Nanofibers as an Efficient Electrode Material for Supercapacitors. *ACS Nano* **2012**, *6*, 7092–7102.
29. Yu, D.; Zhang, Q.; Dai, L. Highly Efficient Metal-Free Growth of Nitrogen-Doped Single-Walled Carbon Nanotubes on Plasma-Etched Substrates for Oxygen Reduction. *J. Am. Chem. Soc.* **2010**, *132*, 15127–15129.
30. Xue, Y.; Liu, J.; Chen, H.; Wang, R.; Li, D.; Qu, J.; Dai, L. Nitrogen-Doped Graphene Foams as Metal-Free Counter Electrodes in High-Performance Dye-Sensitized Solar Cells. *Angew. Chem., Int. Ed.* **2012**, *51*, 12124–12127.
31. Sheng, Z.-H.; Shao, L.; Chen, J.-J.; Bao, W.-J.; Wang, F.-B.; Xia, X.-H. Catalyst-Free Synthesis of Nitrogen-Doped Graphene via Thermal Annealing Graphite Oxide with Melamine and Its Excellent Electrocatalysis. *ACS Nano* **2011**, *5*, 4350–4358.
32. Sharifi, T.; Hu, G.; Jia, X.; Wagberg, T. Formation of Active Sites for Oxygen Reduction Reactions by Transformation of Nitrogen Functionalities in Nitrogen-Doped Carbon Nanotubes. *ACS Nano* **2012**, *6*, 8904–8912.
33. Qu, L.; Liu, Y.; Baek, J.-B.; Dai, L. Nitrogen-Doped Graphene as Efficient Metal-Free Electrocatalyst for Oxygen Reduction in Fuel Cells. *ACS Nano* **2010**, *4*, 1321–1326.
34. Wen, Z.; Wang, X.; Mao, S.; Bo, Z.; Kim, H.; Cui, S.; Lu, G.; Feng, X.; Chen, J. Crumpled Nitrogen-Doped Graphene Nanosheets with Ultrahigh Pore Volume for High-Performance Supercapacitor. *Adv. Mater.* **2012**, *24*, 5610–5616.
35. Gao, Y.; Hu, G.; Zhong, J.; Shi, Z.; Zhu, Y.; Su, D. S.; Wang, J.; Bao, X.; Ma, D. Nitrogen-Doped sp^2-Hybridized Carbon as a Superior Catalyst for Selective Oxidation. *Angew. Chem., Int. Ed.* **2013**, *52*, 2109–2113.
36. Long, J.; Xie, X.; Xu, J.; Gu, Q.; Chen, L.; Wang, X. Nitrogen-Doped Graphene Nanosheets as Metal-Free Catalysts for Aerobic Selective Oxidation of Benzylic Alcohols. *ACS Catal.* **2012**, *2*, 622–631.
37. Marconcini, P.; Cresti, A.; Triozon, F.; Fiori, G.; Biel, B.; Niquet, Y.-M.; Macucci, M.; Roche, S. Atomistic Boron-Doped Graphene Field-Effect Transistors: A Route toward Unipolar Characteristics. *ACS Nano* **2012**, *6*, 7942–7947.
38. Gong, K.; Du, F.; Xia, Z.; Durstock, M.; Dai, L. Nitrogen-Doped Carbon Nanotube Arrays with High Electrocatalytic Activity for Oxygen Reduction. *Science* **2009**, *323*, 760–764.
39. Shin, W. H.; Jeong, H. M.; Kim, B. G.; Kang, J. K.; Choi, J. W. Nitrogen-Doped Multiwall Carbon Nanotubes for Lithium Storage with Extremely High Capacity. *Nano Lett.* **2012**, *12*, 2283–2288.
40. Shao, Y.; Wang, X.; Engelhard, M.; Wang, C.; Dai, S.; Liu, J.; Yang, Z.; Lin, Y. Nitrogen-Doped Mesoporous Carbon for Energy Storage in Vanadium Redox Flow Batteries. *J. Power Sources* **2010**, *195*, 4375–4379.
41. Wang, S.; Zhao, X.; Cochell, T.; Manthiram, A. Nitrogen-Doped Carbon Nanotube/Graphite Felts as Advanced Electrode Materials for Vanadium Redox Flow Batteries. *J. Phys. Chem. Lett.* **2012**, *3*, 2164–2167.
42. Lai, L.; Potts, J.; Zhan, D.; Wang, L.; Poh, C. K.; Tang, C.; Gong, H.; Shen, Z.; Lin, J.; Ruoff, R. Exploration of the Active Center Structure of Nitrogen-Doped Graphene-Based Catalysts for Oxygen Reduction Reaction. *Energy Environ. Sci.* **2012**, *5*, 7936–7942.
43. Marcano, D. C.; Kosynkin, D. V.; Berlin, J. M.; Sinitskii, A.; Sun, Z.; Slesarev, A.; Alemany, L. B.; Lu, W.; Tour, J. M. Improved Synthesis of Graphene Oxide. *ACS Nano* **2010**, *4*, 4806–4814.
44. Paredez, P.; Maia da Costa, M. E. H.; Zagonel, L. F.; Ribeiro, C. T. M.; Alvarez, F. Growth of Nitrogenated Fullerene-Like Carbon on Ni Islands by Ion Beam Sputtering. *Carbon* **2007**, *45*, 2678–2684.
45. Gueorguiev, G. K.; Neidhardt, J.; Stafstrom, S.; Hultman, L. First-Principles Calculations on the Curvature Evolution and Cross-Linkage in Carbon Nitride. *Chem. Phys. Lett.* **2005**, *410*, 228–234.
46. Li, X.; Wang, H.; Robinson, J. T.; Sanchez, H.; Diankov, G.; Dai, H. Simultaneous Nitrogen Doping and Reduction of Graphene Oxide. *J. Am. Chem. Soc.* **2009**, *131*, 15939–15944.
47. Cançado, L. G.; Jorio, A.; Ferreira, E. H. M.; Stavale, F.; Achete, C. A.; Capaz, R. B.; Moutinho, M. V. O.; Lombardo, A.; Kulmala, T. S.; Ferrari, A. C. Quantifying Defects in Graphene via Raman Spectroscopy at Different Excitation Energies. *Nano Lett.* **2011**, *11*, 3190–3196.
48. Panchokarla, L. S.; Subrahmanyam, K. S.; Saha, S. K.; Govindaraj, A.; Krishnamurthy, H. R.; Waghmare, U. V.; Rao, C. N. R. Synthesis, Structure, and Properties of Boron- and Nitrogen-Doped Graphene. *Adv. Mater.* **2009**, *21*, 4726–4730.
49. Wakeland, S.; Martinez, R.; Grey, J. K.; Luhrs, C. C. Production of Graphene from Graphite Oxide Using Urea as Expansion−Reduction Agent. *Carbon* **2010**, *48*, 3463–3470.
50. Podsiadło, S. Stages of the Synthesis of Indium Nitride with the Use of Urea. *Thermochim. Acta* **1995**, *256*, 375–380.

51. Sakata, Y.; Yoshimoto, K.; Kawaguchi, K.; Imamura, H.; Higashimoto, S. Preparation of a Semiconductive Compound Obtained by the Pyrolysis of Urea under N2 and the Photocatalytic Property under Visible Light Irradiation. *Catal. Today* **2011**, *161*, 41–45.
52. Liu, J.; Zhang, T.; Wang, Z.; Dawson, G.; Chen, W. Simple Pyrolysis of Urea into Graphitic Carbon Nitride with Recyclable Adsorption and Photocatalytic Activity. *J. Mater. Chem.* **2011**, *21*, 14398–14401.
53. Guo, B.; Liu, Q.; Chen, E.; Zhu, H.; Fang, L.; Gong, J. R. Controllable N-Doping of Graphene. *Nano Lett.* **2010**, *10*, 4975–4980.
54. Casanovas, J.; Ricart, J. M.; Rubio, J.; Illas, F.; Jiménez-Mateos, J. M. Origin of the Large N 1s Binding Energy in X-ray Photoelectron Spectra of Calcined Carbonaceous Materials. *J. Am. Chem. Soc.* **1996**, *118*, 8071–8076.
55. Pels, J. R.; Kapteijn, F.; Moulijn, J. A.; Zhu, Q.; Thomas, K. M. Evolution of Nitrogen Functionalities in Carbonaceous Materials during Pyrolysis. *Carbon* **1995**, *33*, 1641–1653.
56. Bard, A. J.; Faulkner, L. R. *Electrochemical Methods: Fundamentals and Applications*; John Wiley & Sons, Inc.: New York, 2001; pp 260−261.
57. Liu, G.; Li, X.; Lee, J.-W.; Popov, B. N. A Review of the Development of Nitrogen-Modified Carbon-Based Catalysts for Oxygen Reduction at USC. *Catal. Sci. Technol.* **2011**, *1*, 207–217.
58. Cruz-Silva, E.; Cullen, D. A.; Gu, L.; Romo-Herrera, J. M.; Muñoz-Sandoval, E.; López-Urías, F.; Sumpter, B. G.; Meunier, V.; Charlier, J.-C.; Smith, D. J.; *et al.* Heterodoped Nanotubes: Theory, Synthesis, and Characterization of Phosphorus−Nitrogen Doped Multiwalled Carbon Nanotubes. *ACS Nano* **2008**, *2*, 441–448.